Bioactive Materials 36 (2024) 580–594

Contents lists available at ScienceDirect

Bioactive Materials

journal homepage: www.keaipublishing.com/en/journals/bioactive-materials

Vascular restoration through local delivery of angiogenic factors stimulates bone regeneration in critical size defects

Liang Fang [a], Zhongting Liu [b], Cuicui Wang [a,c], Meng Shi [a], Yonghua He [a], Aiwu Lu [a], Xiaofei Li [a], Tiandao Li [c], Donghui Zhu [d], Bo Zhang [c], Jianjun Guan [b,**], Jie Shen [a,*]

[a] Department of Orthopaedic Surgery, School of Medicine, Washington University, St. Louis, MO, 63110, USA
[b] Department of Mechanical Engineering & Materials Sciences, School of Engineering, Washington University, St. Louis, MO, 63110, USA
[c] Department of Developmental Biology, Center of Regenerative Medicine, Washington University, St. Louis, MO, 63110, USA
[d] Department of Biomedical Engineering, School of Medicine, Stony Brook University, Stony Brook, NY, 11794, USA

ARTICLE INFO

Keywords:
Critical size bone defects
Angiogenesis
Spp1
Cxcl12
Polycaprolactone scaffold

ABSTRACT

Critical size bone defects represent a significant challenge worldwide, often leading to persistent pain and physical disability that profoundly impact patients' quality of life and mental well-being. To address the intricate and complex repair processes involved in these defects, we performed single-cell RNA sequencing and revealed notable shifts in cellular populations within regenerative tissue. Specifically, we observed a decrease in progenitor lineage cells and endothelial cells, coupled with an increase in fibrotic lineage cells and pro-inflammatory cells within regenerative tissue. Furthermore, our analysis of differentially expressed genes and associated signaling pathway at the single-cell level highlighted impaired angiogenesis as a central pathway in critical size bone defects, notably influenced by reduction of Spp1 and Cxcl12 expression. This deficiency was particularly pronounced in progenitor lineage cells and myeloid lineage cells, underscoring its significance in the regeneration process. In response to these findings, we developed an innovative approach to enhance bone regeneration in critical size bone defects. Our fabrication process involves the integration of electrospun PCL fibers with electrosprayed PLGA microspheres carrying Spp1 and Cxcl12. This design allows for the gradual release of Spp1 and Cxcl12 in vitro and in vivo. To evaluate the efficacy of our approach, we locally applied PCL scaffolds loaded with Spp1 and Cxcl12 in a murine model of critical size bone defects. Our results demonstrated restored angiogenesis, accelerated bone regeneration, alleviated pain responses and improved mobility in treated mice.

1. Introduction

Critical size bone defect as one of the most significant orthopedic challenges has been frequently reported in millions of patients each year in the United States and worldwide, associated with substantial healthcare cost and economic burden [1,2]. Various factors can cause critical size bone defect in clinic, including congenital skeletal defects, traumatic injuries, tumor resection, bone resection due to osteomyelitis or previous nonunion [3,4]. Despite the intrinsic tissue regenerative capacity, critical size bone defects always lead to nonunion, therefore resulting at patient disability and dramatically reducing the overall health and life quality for patients. Currently, autologous bone grafts remain the gold standard for treating these defects in clinical practice [5,6]. The demand for bone grafts is substantial, with expenditures exceeding 3 billion dollars in 2019 in costs and projected annual increases of approximately 6 % [7,8]. However, this procedure is substantially hindered by limitations such as restricted availability, including challenges related to shape and the amount that can be harvested. Additionally, alternative approaches utilizing allografts and xenografts are also employed in clinics but with limited success, primarily due to issues such as disease transmission, immune-rejection, and graft failures [9,10]. In recent decades, regenerative medicine and tissue engineering have been extensively studied and hold great promise to improve the treatment of critical size bone defects [2,11,12].

From a perspective of biological regeneration, the failure of critical size bone defect healing arises from multiple components, including

Peer review under responsibility of KeAi Communications Co., Ltd.
* Corresponding author. Department of Orthopaedic Surgery Washington University School of Medicine, St Louis, MO 63110, USA.
** Corresponding author. Department of Mechanical Engineering & Materials Sciences, Washington University School of Engineering St Louis, MO 63130, USA.
E-mail addresses: jguan22@wustl.edu (J. Guan), shen.j@wustl.edu (J. Shen).

https://doi.org/10.1016/j.bioactmat.2024.07.003
Received 5 May 2024; Received in revised form 20 June 2024; Accepted 2 July 2024

deficiencies in growth factors and progenitor cells, as well as the inability to regenerate blood vessels for oxygen and nutrients supply [13–17]. To address these challenges, regenerative osteoprogenitor cells like mesenchymal stem cells and iPSCs (induced pluripotent stem cells), are commonly integrated into biomaterial scaffolds that often supplemented with osteogenic factors such as BMP2 to facilitate local bone formation [18–21]. However, despite advances in stem cell research and biomaterial technology, scaffold-based bone regeneration remains challenging due to concerns such as cell-based immunogenicity, uncontrolled cell differentiation, and interference of the scaffold with crucial cell-cell interactions [22–24]. In addition to cell therapy approaches, significant efforts have been dedicated to engineering microvessel networks for potential clinical applications in recent years [25]. Notably, the discovery of type H vessels directly linking blood vessels and bone formation in the long bone [26], which highlights the importance of stimulating bone regeneration through vascular restoration [27–29]. The combination of three-dimensional (3D) printing with HUVEC cells or iPSC derived endothelial cells has been particularly utilized to predesign the geometry and architecture of the blood vessel network [30–34]. While 3D printing allows for the creation of microvessels with diameter in μm range and precise filamentous resolution, the overall function of these vessels including permeability and perfusability remains poor primarily due to the inherent low cell viability in 3D printing ink and the uncontrolled performance of endothelial cell in vivo [35,36]. Moreover, unlike the artery network, the design of physiologically functional capillary vessels for bone regeneration remains a scientific challenge.

In this regard, leveraging angiogenesis-driven vascularization presents a promising tissue engineering approach for reestablishing the microvessel network crucial for bone regeneration. This strategy allows cells to recapitulate the physiological process of new vessel formation [37,38]. A range of angiogenic factors, including vascular endothelial growth factor (VEGF), monocyte chemoattractant protein 1 (MCP1), and sphingosine 1 phosphate (S1P) as well as exosomes have been utilized in combination with biomaterials to promote the sprouting of HUVECs and facilitate the formation of functional microvessel structures [39–42]. In addition to angiogenic factors, hypoxia-inducible factor 1 (HIF1) has been incorporated into fabricated biomaterials to promote endothelial cell differentiation by inducing the expression of proangiogenic factors, such as VEGF, platelet-derived growth factor (PDGF) and fibroblast growth factor (FGF) under hypoxia conditions [43–46]. Most recently, a novel approach has been developed involving polymer-modified DNA hydrogels containing tetrahedral Framework Nucleic Acid (tFNA) and Aptamer02 (Apt02). This approach simultaneously promotes both angiogenesis and osteogenic mineralization and has demonstrated promising efficacy in bone regeneration in rats with critical size bone defects [47]. However, inconsistent outcomes have also been observed in treatments involving angiogenic factors, particularly regarding blood vessel formation and bone formation in vivo [48,49]. This contradiction primarily arises from a limited understanding of the mechanisms underlying critical size bone defects, which impedes the optimization of tissue engineering products and the development of mechanism-based therapies.

Therefore, we performed single-cell RNA sequencing (scRNA-seq) analysis in this study to explore the cellular and molecular alterations occurring in regenerative tissues from murine critical size bone defects. Our findings confirmed a shift towards fibrotic differentiation rather than normal osteogenic differentiation in the tissue of critical size bone defects, accompanied by elevated inflammatory responses and reduced angiogenesis. To delve deeper into the underlying mechanisms, we separately analyzed progenitor lineage and myeloid lineage, and revealed angiogenesis and neovascularization as most significantly diminished biological functions in both cell lineages. Notably, Spp1 and Cxcl12 emerged as the most decreased angiogenic factors in both progenitor lineage and myeloid lineage cells. These chemokines have been previously documented to recruit endothelial cells and stimulate angiogenesis under both physiological and pathological conditions [50–52]. Furthermore, genetic ablation of Spp1 [53] or Cxcl12 [54] led to impaired angiogenesis and fracture healing, suggesting their positive roles in angiogenesis during the fracture repair process. Therefore, to target the impaired angiogenesis process, we developed FDA-approved polycaprolactone (PCL) scaffolds capable of sustained release of Spp1 and Cxcl12 at the site of bone defects in mice. Remarkably, localized delivery of Spp1 and Cxcl12 accelerated bone formation and alleviated pain responses in mice, underscoring the potential of this approach as a therapeutic strategy for treating critical size bone defects in patients.

2. Materials and methods

2.1. Critical size bone defect model

12-weeks-old male C57BL/6J wild-type mice purchased from The Jackson Laboratory (stock 000664) were used for the critical bone defect model [55]. Briefly, the mice were anesthetized, and the right femur was exposed by maneuvering between the vastus lateralis and biceps femoris longus muscles while ensuring the protection of the sciatic nerve. Two wire saws (RISystem AG, #RIS.590.100) were then carefully placed beneath the femur. Following this, a six-hole plate (RISystem AG, #RIS.401.130) was positioned on the lateral aspect of the femoral stem and secured with screws in both distal and proximal two holes. A jig was attached to the nail tail's end, and the wire saws were threaded into the slots set in the jig to create a specific bone defect size (1 mm defect and 3 mm defect). Subsequently, the synthesized scaffold was wrapped around the defect area, followed by sequential suturing of the muscles and skin.

2.2. scRNA-seq and data processing

The regenerative tissues from the defect gap were harvested at 3 weeks post-surgery and dissociated in 2 mg/mL Collagenase P (Roche, #11249002001) and 2 mg/mL pronase (Millipore Sigma, #10165921001) at room temperature for 1 h. The erythrocytes were removed using anti-GYPA (MyBioSource, #MBS209s3646) and Streptavidin Microbubbles (AKADEUM, #11110-000). Subsequently, the cell suspension was filtered through a 30-μm strainer to yield a single-cell suspension [56]. Two sets of single-cell libraries were prepared: one from cells derived from a 1 mm bone defect (control, $n = 3$) and the other from cells obtained from a 3 mm bone defect (nonunion, $n = 3$). For each sample, ten thousand cells were loaded for processed to generate single-cell mRNA libraries using the Chromium Single Cell 3′ kit (v3.1 Chemistry, 10 × Genomics Inc). These libraries were barcoded, purified, and sequenced in a 2 × 150-bp paired-end configuration on an Illumina NovaSeq platform. CellRanger pipeline (v7.0.1, https://support.10xgenomics.com/single-cell-gene-expression/software/pipelines/latest/using/what-is-cell-ranger) was utilized to align reads, extract cell barcodes and unique molecular identifier (UMI) counts, and generate feature-barcode matrices. The reads were mapped to the mouse (mm10) reference genome following the standard workflow of 10 × Genomics.

2.3. scRNA-seq analysis

Quality control was conducted for each dataset. Multiplets or cells with poor quality defined by UMI counts below 5000 or exceeding 60,000, features below 2000 or above 5,000, or mitochondrial UMIs percentages exceeding 8 %, were excluded from further analysis. Integration of datasets was performed using Seurat v4.3.0 [57]. Feature data was normalized using the Seurat NormalizeData function, employing global-scaling normalization, followed by scaling using the Seurat ScaleData function to mitigate variations from unwanted sources for downstream analyses. Nonlinear dimensional reduction was achieved with t-distributed stochastic embedding (tSNE) and graph-based clustering was performed using the Louvain algorithm. The top 12

statistically significant principal components were chosen empirically, guided by testing the top 10 differentially expressed genes (DEGs) using Wilcox's method among clusters. Cell clusters annotation was performed by examining cell type–specific marker gene expression across clusters. Gene Ontology (GO) enrichment analysis was performed using ToppGene Suite [58] with Benjamini-Hochberg (B&H) correction less than 0.05. DEGs of interest identified from Seurat analysis were uploaded as the input seed and overlayed with global biological processes from the GO: Biological Process (GO: BP) database to identify significant BP terms. Enrichment p-values were calculated using hypergeometic probability mass function and adjusted using B&H correction. Gene set enrichment analysis (GSEA) [59] was performed using GSEA software (v4.3.2). The normalized expression data was retrieved and subset for progenitor lineage (clusters 1, 4, and 5) and myeloid lineage (clusters 0, 8, and 10), respectively. GSEA was performed separately with the expression dataset of progenitor lineage and myeloid lineage for the identification of enriched functions affected by critical size bone defects. The normalization mode was set to meandiv. Only those gene set with a size of more than 15 genes were retained for further analysis. Hallmark gene sets from the Molecular Signature Database (MSigDB) were used as gene sets. A *q*-value cut-off of 0.05 was used to select statistically significant enriched functions.

2.4. Histological analyses

The femurs ($n = 5$) were collected for histological assessment at 4 and 10 weeks post-surgery After fixation in 10 % neutral buffered formalin and decalcification with 14 % ethylenediaminetetraacetic acid (EDTA), the femurs were embedded in paraffin, sectioned at 5 μm thickness, and stained with Alcian blue/Hematoxyline/Orange G (ABH/OG) and tartrate-resistant acid phosphatase (TRAP) [60,61] as well as Masson's Trichrome to analyze the composition of regenerative tissue and osteoclast formation in regenerative tissue. Immunofluorescence staining for Spp1 (1:50, Abcam, #ab8448), Cxcl12 (1:50, LSBio, #LS-B2437), Endomucin (1:100, Santa Cruz, #sc-65495), and CD31 (1:100, BD Biosciences, #550274) was performed via proteinase K antigen retrieval and fluorescent development using an Alexa Fluor 488 or Alexa Fluor 594 antibody labeling kit (Thermo Fisher, #A20181 or #A20185). IHC staining for type III collagen (1:500, Abcam, #ab7778) was performed by proteinase K antigen retrieval and DAB (3,3′-diaminobenzidine, Vector Laboratories, #SK4100) mediated colorimetric development.

2.5. Micro-CT analyses

To monitor the progression of bone formation in mice, VivoCT 40 scanner (Scanco) was used to scan the surgical femur every two weeks following the surgery. The scanning parameters were set to 70 kV, 114 μA, and a 300 ms integration time. Bone formation rate was determined by analyzing the closure of the bone defect gap per week, as observed in the in vivo microCT scans over a period of 10 weeks. At the end time point, the femur was dissected at 10 weeks post-surgery and examined using a micro-CT scanner (uCT50, Scanco) with the following parameters: 55 kV, 145 μA, and a 300 ms integration time. Three-dimensional images were generated using Scanco software. Quantifications of bone volume fraction (BV/TV) was performed on 600 slices centered on the midpoint of the bone defect area, as previously described [62].

2.6. Animal behavioral tests

The pain response and mobility of mice were evaluated at 10 weeks post-surgery. Electronic Von Frey (BIOSEB, #BIO-EVF4) was used to assess the mechanical sensitivity threshold in mice following critical size bone defect surgeries. The electronic probe was applied to the central area of murine hind paws to induce nociceptive pain, and the stimulus intensity was automatically recorded upon paws withdrawal. Additionally, bone defect related local pain was evaluated in mice using a Small Animal Algometer (SMALGO; BIOSEB, #BIO-SMALGO). This involved the application of progressively increasing force at a rate of 50 g/s to both uninjured and injured femurs, with force levels automatically recorded until limb withdrawal. 450 g was the maximum force applied to prevent tissue damage. For both Von Frey and SMALGO assays, each mouse underwent three measurements, which were then averaged to obtain a final readout. Furthermore, the activity of the mice over a two-day period was monitored and analyzed using spontaneous activity wheels (BIOSEB, #BIO-ACTIVW-M). Parameters such as travel distance, average and maximum speed and total time spent on the wheel were recorded for each individual mouse.

2.7. Fabrication and characterization of Spp1 and Cxcl12 releasing scaffolds

The scaffolds were fabricated by simultaneously electrospinning polycaprolactone (PCL) fibers and coaxially electrospraying of poly (D,L-lactide-*co*-glycolide) (PLGA) microspheres containing Spp1 and Cxcl12. The PCL solution (Sigma-Aldrich, #440744) was prepared at a concentration of 10 wt% in chloroform, while PLGA (LACTEL, #B6010-4) was dissolved in dichloromethane at a concentration of 5 wt%. Three growth factor solutions were utilized, specifically 280 μg/mL Spp1, 180 μg/mL Spp1, 120 μg/mL Spp1, 70 μg/mL Cxcl12, 50 μg/mL Cxcl12, 30 μg/mL Cxcl12, 280 μg/mL Spp1 + 70 μg/mL Cxcl12, 180 μg/mL Spp1 + 50 μg/mL Cxcl12, and 120 μg/mL Spp1 + 30 μg/mL Cxcl12.

The PCL solution stream was charged positively at +18 kV and delivered at a rate of 5 mL/h [56,63–65]. Coaxial electrospraying was performed using a coaxial device with inner and outer needles of diameters 0.7 mm and 1.65 mm, respectively. The PLGA solution was pumped through the outer needle at 1.2 mL/h, while the growth factor solution was pumped through the inner needle at 0.2 mL/h. The coaxial device was charged at +24 kV. The distance between the tip of the PCL solution needle and the collecting mandrel, as well as between the coaxial device tip and the collecting mandrel, was set at 20 cm. The mandrel, rotating at a speed of 600 rpm, was negatively charged at −10 kV. The fabrication process was sustained for 30 min, following which the scaffold was harvested from the mandrel. Scaffold without growth factors was also fabricated and used as a control. The morphology of scaffold was characterized using a scanning electron microscope.

2.8. In vitro and in vivo growth factor release from scaffolds

To evaluate in vitro growth factor release, 25 mg of scaffold was placed in 500 μL of PBS and maintained at 37 °C for a duration of 28 days. At predefined time intervals, the supernatant was collected, and an equivalent volume of fresh PBS was added. The concentrations of released growth factors in the supernatant were determined using ELISA kits for Spp1 (PeproTech, #120-35) and Cxcl12 (PeproTech, #300-28A) [65]. Three biological repeats were included in each experiment.

For the assessment of in vivo growth factor release, the scaffolds were surgically implanted in murine femurs. Briefly, a critical size bone defect was created in murine femurs, and the broken bones were stabilized using platinum plates and screws. Scaffolds with a width of 4 mm were immediately wrapped around the surgically created gap region. The muscles were then closed with sutures to ensure the scaffolds remained stable in the gap region. Following implantation, at intervals of 3 and 14 days, the scaffolds (n = 3) were removed, and any adhering tissues were carefully removed. Subsequently, the scaffolds were incubated in PBS until ELISA assays indicated no further release of growth factors from the scaffolds, a period spanning over 7 weeks. The percentage of in vivo growth factor release was calculated based on the amount released in vitro relative to the amount initially loaded into the scaffolds.

2.9. Endothelial cell migration and tube formation assays

To investigate the impact of different scaffolds on endothelial cell migration and tube formation in vitro, a collagen gel model was utilized [65]. The scaffold was positioned at the bottom of a 24-well plate, and 160 μl of collagen solution (CORNING, #354236) was layered on top of the scaffold. Following incubation at 37 °C for 1 h to allow the solidification of the collagen solution, human umbilical vein endothelial cells (HUVECs) labeled with live cell tracker CM-Dil (Invitrogen by Thermo Fisher Scientific, #C7000) were seeded onto the collagen gel at a density of 1×10^5 cells/mL. The plates were then incubated at 37 °C. After 5 days, the cells were fixed with a 4 % paraformaldehyde solution (Thermo Fisher Scientific, #J19943-K2). There were three biological repeats in each culture condition. The migration of cells into the collagen gel was visualized using a confocal microscope. Z-stack images were captured at a thickness of 20 μm and subsequently reconstructed to generate 3D images. The number of migrated cells and lumen density were determined based on these images.

2.10. Osteoblast cells isolation and culture

Primary osteoblast cells were isolated from the calvarias of new born C57BL/6J wild type mice. Briefly, calvarias were collected by carefully removing the soft tissue and sutures, followed by digestion with 0.1 % dispase (Sigma, #D4693) and 0,1 % collagenase P (Sigma, #11249002001). The osteoblast cells were then stimulated with 50 μg/mL ascorbic acid (Sigma, #57803) for maturation before treatment with Spp1 and Cxcl12 (n = 3) for 24 h. RNA was collected for real-time qPCR to assess the gene expression levels of *Runx2*, *Alp* and *Actb*. The primer sequences for real-time qPCR were as follows: *Runx2*, forward: 5′-CGTCCACTGTCACTTTAATAGCTC-3′, and reverse: 5′-GTAGCCAGGTTCAACGATCTG-3’; *Alp*, forward: 5′-TGACCTTCTCTCCTCCATCC-3′, and reverse: 5′-CTTCCTGGGAGTCTCATCCT-3’; *Actb*, forward: 5′-AGATGTCCATCAGCAAGCAG-3′, and reverse: 5′-GCGCAAGTTAGGTTTTGTCA-3’.

2.11. Statistics

All data were analyzed using GraphPad Prism and were presented as mean ± SD from a minimum of three independent experiments. Significance between two groups was determined using a 2-tailed Student’s *t*-test. For comparison among multiple groups, a two-way analysis of variance (ANOVA) was used, followed by pairwise comparisons via Tukey’s test. Statistical significance was defined as a p value less than 0.05.

3. Results and discussion

3.1. Altered cellular composition and molecular signatures in critical size bone defects

Bone regeneration is a complicated and intricately orchestrated process involving multiple cell lineages. However, our current understanding of this process remains limited, posing a significant obstacle to the advancement of tissue engineering applications in treating critical size bone defects. To address this knowledge gap, our study adopted a mechanistic approach, aiming to comprehensively understand the cellular and molecular events that govern microenvironment within regenerative tissue following critical size bone defects. We compared the bone regeneration process in a well-established murine 3 mm bone defects model to a 1 mm bone defects. Recognizing the complexity and heterogeneity of regenerative tissue, we utilized single-cell RNA-seq to identify and profile individual cells, enabling us to unravel how critical size bone defects alter the cellular and molecular programs involved in bone regeneration. To maintain the integrity of the cell population and minimize unnecessary contamination of original bone cells, we isolated the regenerative tissues within the defect gap after carefully removing the muscle and other soft tissue (Fig. S1). The entire cell population localized in the regenerative tissues was released through 1-h enzymatic digestion at room temperature for subsequent single-cell RNA sequencing (scRNA-seq). Our scRNA-seq analysis, employing an unbiased clustering approach, revealed sixteen distinct cellular clusters with unique gene expression signatures (Fig. 1A–C, S2 and S3A). In particular, three major cell populations were further identified: (a) three progenitor lineage subsets characterized by the expression of *Prrx1* and stem cell antigen 1 (*Sca1/Ly6a*) [66], (b) four myeloid lineage subsets characterized by the expression of myeloid marker *Cd68* [67], and (c) one endothelial lineage subsets characterized by the expression of *Pecam1/Cd31*, and pan-endothelial marker VE-cadherin (*Cdh5*) [68] (Fig. 1B). Consistent with prior clinical observations and rodent models [2], our scRNA-seq analysis demonstrated a decrease in progenitor lineage cells and endothelial cells, alongside an increase in fibrotic lineage cells and pro-inflammatory cells within regenerative tissue (Fig. 1D). Specifically, the population of progenitor lineage cells drastically decreased from approximately 37.5 % in 1 mm bone defects to around 6.4 % in 3 mm bone defects. Endothelial cells were largely depleted with only about 3 % remaining in 3 mm bone defects (Fig. 1E). Moreover, inflammatory cells including inflammatory T cells (clusters 2) and B lymphocytes (clusters 7, 11, and 14) were significantly expanded, comprising more than 50 % of cells in 3 mm bone defects compared to 10 % in 1 mm bone defects. Conversely, anti-inflammatory cells (M2 macrophages, cluster 0) were significantly decreased from 16 % in 1 mm bone defects to 4.1 % in 3 mm bone defects (Fig. 1E). The expression levels of pro-inflammatory cytokines, such as IL-1β, IL12, TNF-α and IFN-γ were significantly elevated in these cells (Fig. S3B), indicating heightened immune response activation and persistent chronic inflammation. Altogether, these data suggest that critical size bone defects result in a compromised microenvironment characterized by reduced blood vessels, leading to nutritional and oxygen stress, coupled with elevated inflammatory conditions and mechanical stress.

3.2. Diminished angiogenesis mediated by reduction of Spp1 and Cxcl12 in critical size bone defects

In addition to the evaluation of cellular composition alterations, we conducted an analysis of differentially expressed genes and associated signaling pathway in individual cells of regenerative tissues. Our focus was particularly on populations showing the most profound cellular alterations, notably within progenitor lineage and myeloid lineage. These two cell populations, particularly Prrx1 progenitors and M2 macrophages are crucial in restoring microenvironment homeostasis and regulating the bone regeneration [69]. Within the progenitor lineage, we observed three distinct cell types in progenitor lineage based on lineage-specific gene signatures (Fig. 1A–C, S2 and S3), e.g., Prrx1+ progenitors (cluster 4), Osteo-chondro progenitors (cluster 1), and MSC-like fibroblasts/fibroblast precursors (cluster 5). We employed Gene Ontology (GO) enrichment analysis to overview the altered signaling pathways particularly in cluster 4 and 5, respectively. Cluster 1 was not included due to insufficient cells (7 cells) remaining in 3 mm bone defects, which could potentially hinder the robustness of comparison between two conditions. Notably, we identified several distinct pathways that were altered in each individual cell lineage under critical size bone defects. For instance, biological processes and canonical pathways associated with progenitor cell proliferation, osteogenic differentiation and angiogenesis were significantly decreased in Prrx1+ progenitors (Fig. 2A and S4A-B). Similarly, 3 mm bone defects reduced the processes related to angiogenesis, blood vessel development, skeletal tissue (bone and cartilage) development, as well as energy metabolism (e.g., oxidative phosphorylation) that is crucial for osteoblast differentiation in MSC-like fibroblast/fibroblast precursors (Fig. 2B and S4C-D). As anticipated, GO analysis of M2 macrophage cells revealed an increased myeloid cell differentiation and elevated inflammatory

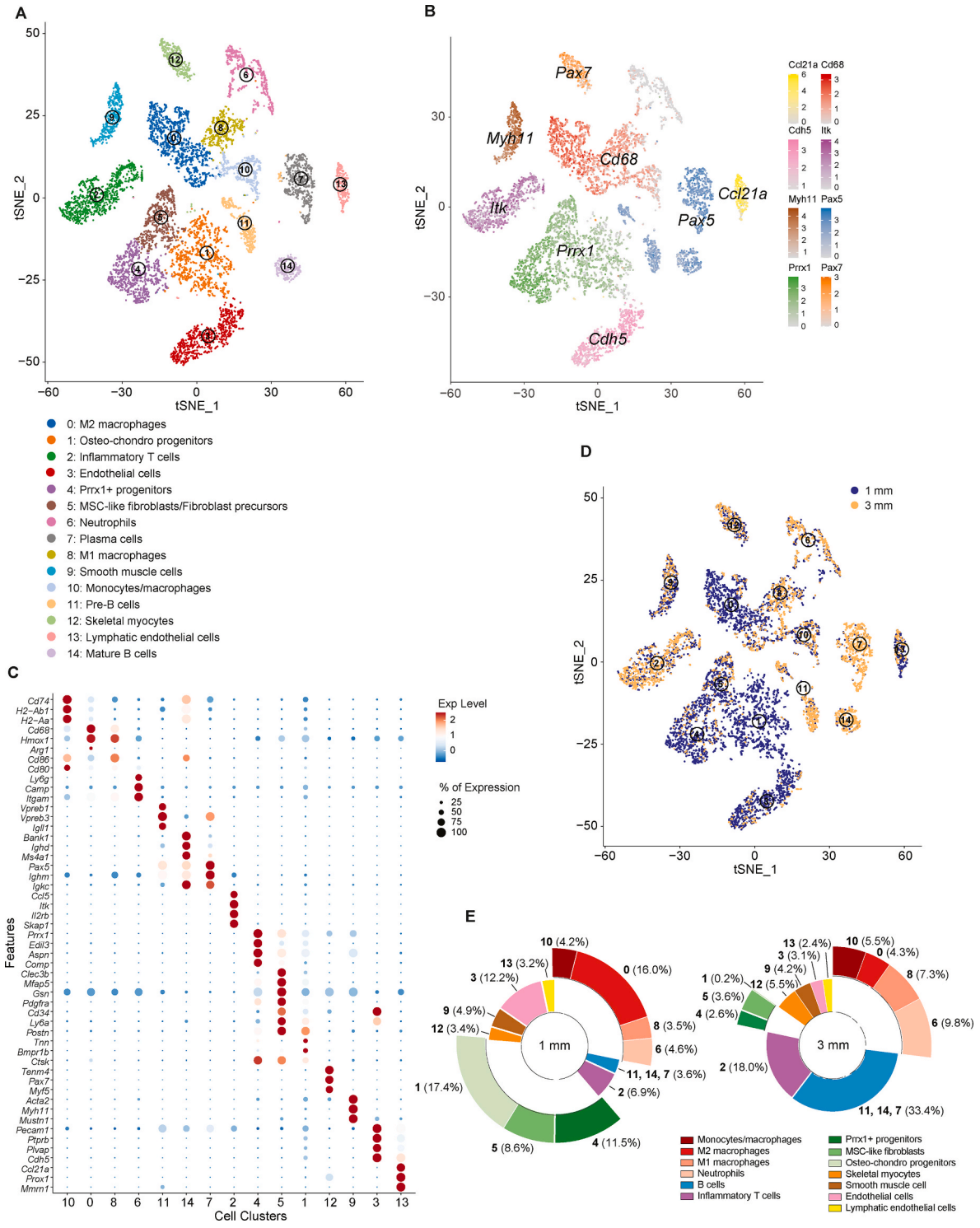

Fig. 1. scRNA-seq analysis of regenerative tissues from murine critical size bone defects. Sixteen cell clusters of regenerative tissues from control (1 mm defect) and critical size bone defects (3 mm defect) at 3 weeks post-surgery (n = 3). A tSNE projection of 9569 single-cell transcriptomes, annotated post hoc and colored by (**A**) clustering, or by expression of (**B**) selected marker genes. (**C**) Dot plots to visualize the changes of key feature expression across cell clusters. The size scale of the dots represents the percentage of cells within a cluster, while the color scale represents the average expression level across all cells within a cluster. (**D**) The tSNE plot colored by different groups. Blue: control (1 mm defect). Yellow: critical size bone defects (3 mm defect). (**E**) Cell fractions of each cell cluster in regenerative tissues from control and critical size bone defects shown by pie charts.

responses in regenerative tissues from 3 mm bone defects. In comparison, M2 macrophages showed a reduced capacity to suppress inflammatory activation in regenerative tissues from 3 mm bone defects (Fig. 2C and S4E-F).

We then performed unbiased Gene Set Enrichment Analysis (GSEA) to identify functional gene sets from a broad spectrum of differentially expressed genes, allowing us to gain deeper insights into the functional pathways and biological processes underlying the observed alterations in gene expression within the regenerative tissues. Remarkably, compared to 1 mm bone defects, two gene sets associated with

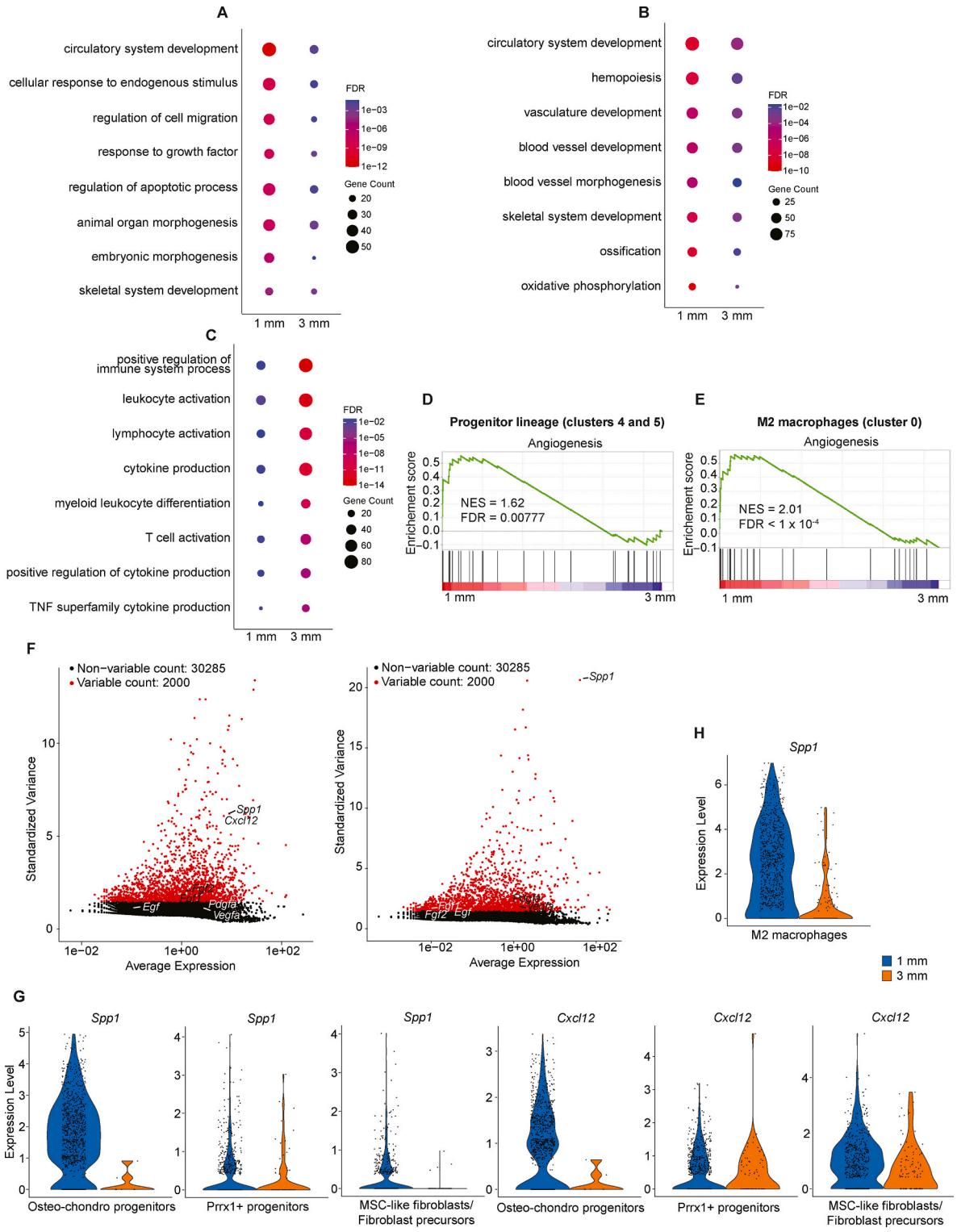

Fig. 2. Reduced angiogenesis in murine critical size bone defects. GO term enrichment analysis showing progenitor cells in (**A**) cluster 4 and (**B**) cluster 5 with bone regeneration and angiogenesis related pathways downregulated, while (**C**) M2 macrophages with inflammation related pathways upregulated in 3 mm bone defect regenerative tissue. GSEA plot showing that angiogenesis was significantly decreased in (**D**) progenitor lineage cells and (**E**) myeloid lineage cells of critical size bone defects. NES, normalized enrichment score; FDR *q*-value as indicated in the plot. (**F**) Identification of highly variable features. Gene variant analysis plot showing *Spp1* and *Cxcl12* as most altered genes related to angiogenesis in progenitor lineage. Each dot represents a gene with red exhibiting high cell-to-cell variation and black dot showing minimal variance among cells of comparison. Violin plots of *Spp1* and *Cxcl12* expression in (**G**) progenitors and (**H**) M2 macrophages.

angiogenesis and oxidative phosphorylation, respectively were significantly decreased in progenitor lineage (cluster 4 and 5) in 3 mm bone defects (Fig. 2D and S5A). In M2 macrophages, three gene sets associated with angiogenesis, interferon gamma response and TNFα signaling via NFκB were reduced in 3 mm bone defects (Fig. 2E and S5B). These findings underscore the impaired angiogenesis as a central pathway in critical size bone defects, with pronounced enrichment observed in the two most significantly altered cell lineages, e.g., progenitor lineage cells and M2 macrophages. To pinpoint the most altered genes related to angiogenesis, we conducted a gene variant analysis and identified Secreted phosphoprotein 1 (*Spp1*) as the most variant feature in M2 macrophages, and CXC motif chemokine ligand 12 (*Cxcl12*) in progenitor lineage cells (Fig. 2F). Interestingly, commonly utilized angiogenic factors in tissue engineering, such as Vegf, Fgf and Pdgf showed either no significant alterations or minimally changes in critical size bone defects (Fig. 2F). Violin plot data further demonstrated significantly

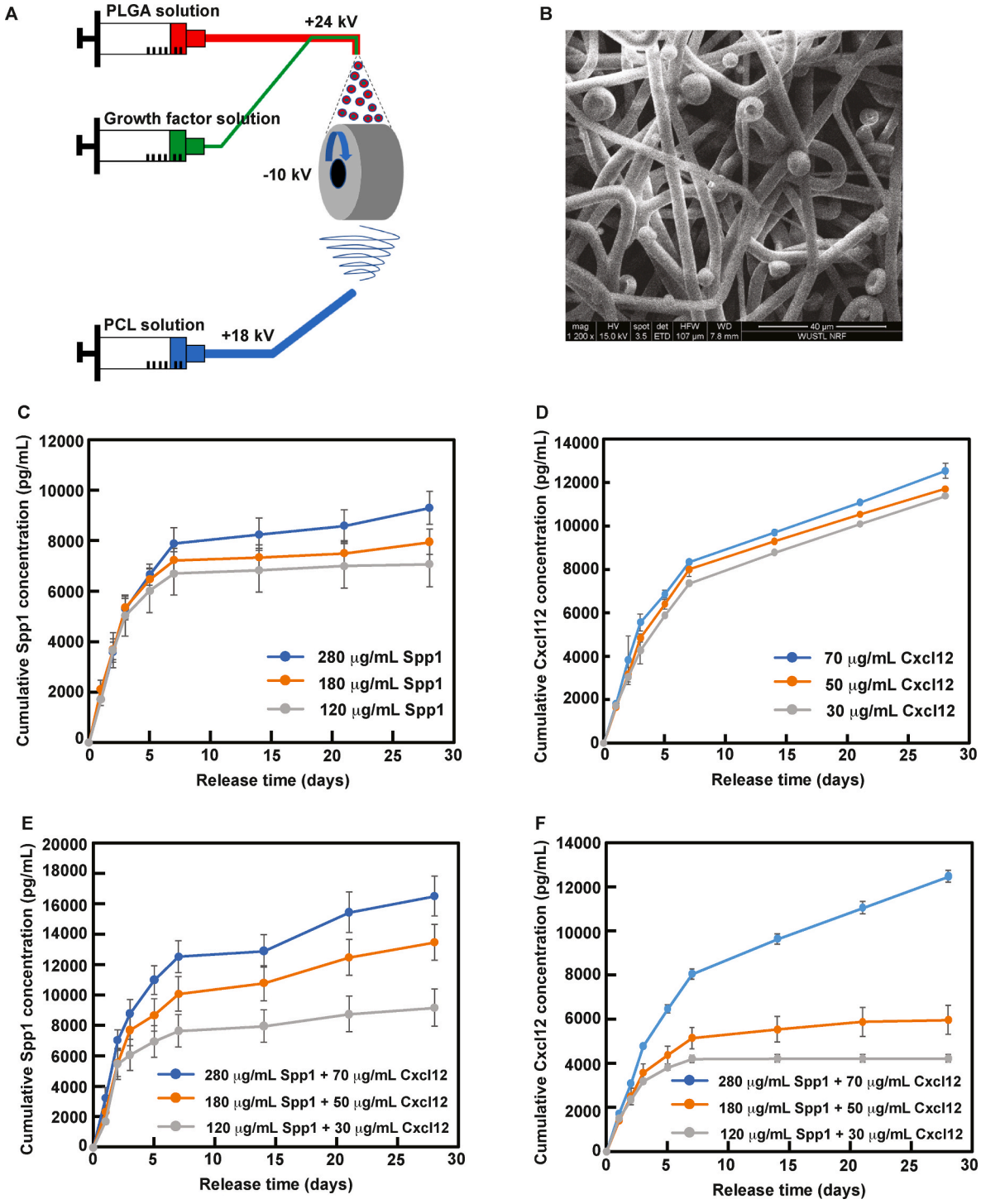

Fig. 3. Fabrication and characterization of PCL scaffold for sustained release of Spp1 and Cxcl12. (**A**) Schematic illustration of the simultaneous electrospinning and electrospraying system for PCL scaffold fabrication. (**B**) Representative SEM images of the PCL scaffold. (**C**) Release profiles of Spp1 from PCL scaffolds loaded with Spp1 (n = 3). (**D**) Release profiles of Cxcl12 from PCL scaffolds loaded with Cxcl12 (n = 3). Release profiles of (**E**) Spp1 and (**F**) Cxcl12 from PCL scaffolds loaded with both factors (n = 3). Data presented as mean ± SD. *$p < 0.05$ by 2-way ANOVA followed by Tukey's test.

reduced expression levels of *Spp1* and *Cxcl12* in progenitor cells (Fig. 2G) and M2 macrophages (Fig. 2H). This highlights the crucial role of Spp1 and Cxcl12 mediated angiogenesis in regulating the homeostatic microenvironment essential for progenitor cell recruitment, proliferation, and differentiation during bone regeneration. Furthermore, we performed immunofluorescent staining and confirmed the diminished expression levels of Spp1 and Cxcl12 in critical size defect tissues (Fig. S6). These findings provide valuable insights into potential therapeutic targets for enhancing bone regeneration process in critical size defects.

3.3. Fabrication of biodegradable scaffolds for sustained release of Spp1 and Cxcl12

With our mechanistic studies providing valuable insights into potential therapeutic targets for enhancing bone regeneration process in critical size defects, we proceeded to engineer scaffolds specifically designed to gradually release Spp1 and Cxcl12. These scaffolds were made from polycaprolactone (PCL), an FDA-approved biodegradable polyester that has been used in tissue regeneration [70]. Employing an innovative fabrication approach that combines electrospinning and electrospraying (Fig. 3A), we successfully integrated electrospun PCL fibers with electrosprayed PLGA microspheres, carrying either Spp1,

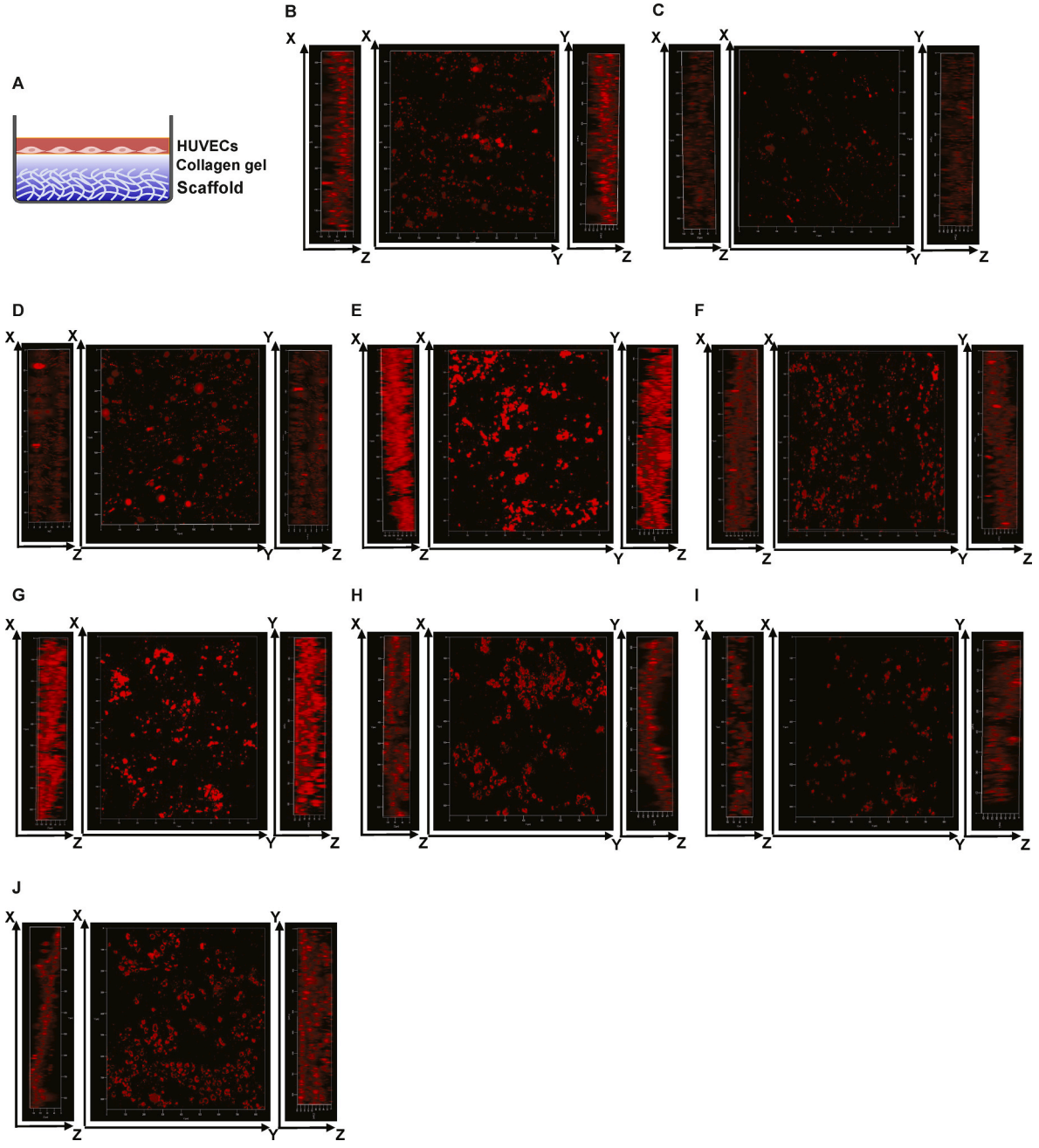

Fig. 4. Effects of Spp1 and Cxcl12 released from PCL scaffolds on endothelial cell migration. (**A**) Schematic representation of endothelial cell migration and morphogenesis experiments in cell cultures. Reconstructed 3D images of HUVECs migrated into collagen gels in response to Spp1 and Cxcl12 released from PCL scaffolds. HUVECs migrated in response to (**B**) 280 μg/mL Spp1; (**C**) 70 μg/mL Cxcl12; (**D**) 280 μg/mL Spp1 + 70 μg/mL Cxcl12; (**E**) 180 μg/mL Spp1; (**F**) 50 μg/mL Cxcl12; (**G**) 180 μg/mL Spp1 + 50 μg/mL Cxcl12; (**H**) 120 μg/mL Spp1; (**I**) 30 μg/mL Cxcl12; and (**J**) 120 μg/mL Spp1 + 30 μg/mL Cxcl12. X: length; Y: width; Z: thickness.

Cxcl12, or a combination of both factors. The structural integrity and composition of these scaffolds were confirmed through scanning electron microscopy (SEM) imaging (Fig. 3B), revealing PCL fiber diameters averaging 7.4 ± 1.0 μm and PLGA microspheres diameters averaging 6.9 ± 0.8 μm, respectively. These analyses revealed that PCL fibers closely mimicked collagen morphology found in murine periosteum, providing a structure with sufficient micropores for cell migration. This similarity suggests that the electrospun PCL scaffolds may offer a suitable microenvironment for promoting cell migration and subsequent tissue regeneration. Additionally, we have previously demonstrated that electrospun PCL scaffolds possess mechanical properties suitable for bone regeneration [56]. The release profiles of Spp1 and Cxcl12 from the scaffolds were then assessed through their incubation in PBS over a duration of 4 weeks. Notably, the release kinetics displayed a biphasic pattern, characterized by an initial rapid release within the first 7 days, followed by a more sustained release extending up to day 28 (Fig. 3C–F). Scaffolds loaded with either Spp1 or Cxcl12 showed variable amounts of growth factors released, dependent on the initial concentrations, with higher concentrations leading to greater release at each interval (Fig. 3C and D). Similarly, scaffolds co-loaded with both growth factors demonstrated dose-dependent release profiles, with increased release correlating with higher initial loadings (Fig. 3E and F).

3.4. Enhanced endothelial cell migration and morphogenesis through co-delivery of Spp1 and Cxcl12

In addition to release profile, we further investigated how the released Spp1 and Cxcl12 from the scaffolds influenced endothelial cell migration and tube formation. To simulate the post-implantation scenario where endothelial cells migrate through a collagen-rich extracellular matrix in response to the released Spp1 and Cxcl12, a layer of collagen gel was placed atop the scaffold, and human umbilical vein endothelial cells (HUVECs) labeled with live cell tracker CMDil were cultured on the collagen gel (Fig. 4A). After 5 days, HUVECs migrated

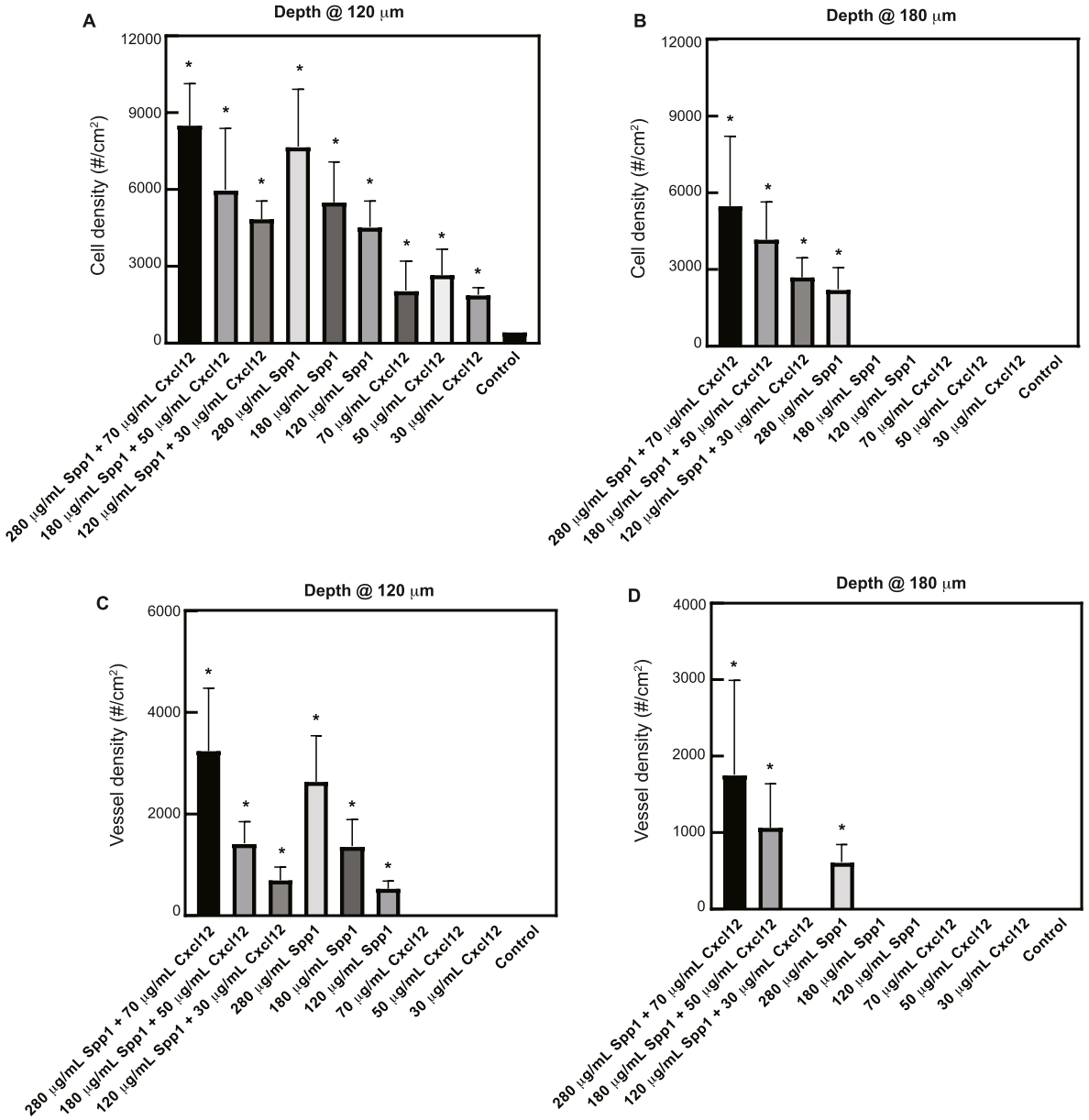

Fig. 5. Effects of Spp1 and Cxcl12 released from PCL scaffolds on vessel formation. The densities of HUVECs migrated to the depths of (**A**) 120 μm and (**B**) 180 μm within collagen gels (n = 3), respectively. The densities of HUVEC lumens formed at depths of (**C**) 120 μm and (**D**) 180 μm within collagen gels (n = 3), respectively. Data presented as mean ± SD. *$p < 0.05$ by 2-way ANOVA followed by Tukey's test.

into the collagen for up to a depth of 120 μm, with the cell density at this depth significantly lower compared to scaffolds containing Spp1, Cxcl12 or both (Fig. 4B–J, 5A, and S7). The density of migrated cells at 120 μm correlated with the initial loading of growth factors within the scaffold. While scaffolds loaded solely with Cxcl12 did not exhibit a significant increase in cell density with escalating initial loading, scaffolds containing only Spp1 showed a significant increase in cell density with an increase in initial loading from 120 μg/mL to 280 μg/mL. Co-delivery of Spp1 and Cxcl12 led to a significant enhancement in cell density compared to scaffolds containing Cxcl12 alone, albeit without a significant difference compared to scaffolds containing only Spp1. Furthermore, scaffolds loaded with higher concentration of both Spp1 and Cxcl12 significantly increased cell density ($p < 0.05$ for 280 μg/mL Spp1 + 70 μg/mL Cxcl12 vs. 120 μg/mL Spp1 + 30 μg/mL Cxcl12). The synergistic effect of co-delivered Spp1 and Cxcl12 was evident in promoting deeper migration of cells into the collagen gel. Cells within scaffolds co-loaded with both growth factors migrated to a depth of 180 μm, whereas this depth was not reached in scaffolds loaded with a single growth factor except for the highest concentration of Spp1 (280 μg/mL). Consistent with results at a depth of 120 μm, scaffolds loaded with higher concentrations of both Spp1 and Cxcl12 significantly increased cell density at a depth of 180 μm (Fig. 5B; $p < 0.05$ for 280 μg/mL Spp1 + 70 μg/mL Cxcl12 vs. 120 μg/mL Spp1 + 30 μg/mL Cxcl12).

We next examined the effect of Spp1 and Cxcl12 release on the tube formation of endothelial cells that had migrated into the collagen gel. At a depth of 120 μm, lumens were exclusively observed in groups where either Spp1 alone or Spp1 in combination with Cxcl12 were released (Fig. 5C). We observed a significant increase in lumen density with higher concentrations of Spp1 in the scaffolds, whether Spp1 was administered alone or in combination with Cxcl12. However, the lumen densities in the groups with both Spp1 and Cxcl12 were comparable to those in groups with equivalent amounts of Spp1 alone. At a depth of 180 μm, lumens formed only in groups with higher concentrations of both Spp1 and Cxcl12 (280 μg/mL Spp1 + 70 μg/mL Cxcl12; 180 μg/mL Spp1 + 50 μg/mL Cxcl12) and in the group with the highest concentration of Spp1 alone (280 μg/mL Spp1) (Fig. 5D). Notably, the group with 280 μg/mL Spp1 and 70 μg/mL Cxcl12 exhibited a significantly higher lumen density than the group with 280 μg/mL Spp1 alone. These findings demonstrate that higher Spp1 release enhances endothelial cell morphogenesis, and the addition of Cxcl12 further amplifies this effect.

3.5. Enhanced bone regeneration in critical size bone defects treated by local sustained release of Spp1 and Cxcl12

Encouraged by the in vitro release profile and functional assessment PCL scaffold loaded with Spp1 and Cxcl12, we proceeded to evaluate the in vivo release profile of Spp1 and Cxcl12 from the scaffolds. Specifically, PCL scaffolds with 280 μg/mL Spp1 and 70 μg/mL Cxcl12 were implanted in mice by wrapping them around the femur bone directly beneath the muscle layer. Following 3 and 14 days post-implantation, the scaffolds retained 69.6 ± 6.1 % and 61.6 ± 6.8 % of Spp1, respectively. Meanwhile, 54.0 ± 1.7 % of Cxcl12 levels remained after 3 days, decreasing to 43.4 ± 17.1 % after 14 days (Table 1). These results demonstrate a sustained release of Spp1 and Cxcl12 from the scaffolds over a period of at least 2 weeks, suggesting their potential utility as therapeutic agents for enhancing bone regeneration in vivo.

Given the potential side effects associated with excessive Spp1 and Cxcl12, such as rheumatoid arthritis, cancer metastasis and malignancy [71–74], we applied this periosteum-like scaffold locally in femurs with critical size bone defects in mice to evaluate the treatment efficacy of the PCL scaffold (Fig. 6A). Over a period of 10 weeks, in-vivo microCT scans revealed a gradual bone regeneration in mice treated with PCL scaffold with either Spp1, Cxcl12, or a combination of both factors, in comparison to mice treated with PCL scaffold alone (Fig. S8). Importantly, treatment with the PCL scaffold alone showed no significant improvement, with a less than 0.1 mm/week bone formation rate observed. However, treatment with either Spp1 or Cxcl12 individually via the PCL scaffold significantly accelerated the bone formation rate in mice with critical size bone defects. Notably, the combined treatment with both factors achieved the highest bone formation rate (approximately 0.25 mm/week) over the 10-week period (Fig. 6B). In addition to the in-vivo microCT scans, we also performed the histological and microCT assessments at 4-week and 10-week post bone defects to examine the tissue compositions in mice. These complementary analyses revealed distinct differences in the regenerative outcomes among the treatment groups (Fig. 6C). Mice treated solely with the PCL scaffold exhibited diminished angiogenesis, as evidence by the absence of Endomucin staining in the regenerative tissue. In contrast, mice treated with angiogenic factors demonstrated evidence of newly formed Endomucin-positive blood vessels (Fig. 6D and E), indicating enhanced angiogenesis. In addition to bone formation-related type H vessels (Endomucin positive), we also detected newly formed CD31 positive vessels in mice treated with angiogenic factors (Fig. S9). Furthermore, mice treated with the PCL scaffold alone exhibited persistent fibrotic scar tissue, evidenced by positive Trichrome staining and type III collagen staining, while those mice treated with angiogenic factors displayed newly formed bone tissue with reduced fibrotic tissue (Fig. S10), suggesting improved bone regeneration. Notably, the combined treatment with both factors resulted in the stimulation of a relatively complete bone bridge in mice with critical size bone defects by 10 weeks post bone defects (Fig. 7A and B), along with active osteoclast-mediated bone remodeling (Fig. S11). This underscores the synergistic effects of angiogenic factors in promoting robust bone regeneration. Previous studies have shown that Spp1 and Cxcl12 have the ability to promote blood vessel formation through MAP kinase pathway in endothelial cells [75,76], therefore, it is plausible that localized treatment of Spp1 and Cxcl12 via PCL scaffold could synergistically induce angiogenesis by activating the MAP kinase pathway. In addition to evaluating the synergistic effects on angiogenesis, we also assessed the osteogenic impact of Spp1 and Cxcl12 on primary osteoblast cells. Consistent with prior reports [77–80], treatment with Spp1 and Cxcl12 significantly induced the expression levels of osteogenic genes, such as *Runx2* and *Alp* (Fig. S12). These data strongly suggest a potential positive feedback regulation between the process of angiogenesis and osteogenesis mediated by Spp1 and Cxcl12, albeit Spp1 may potentially stimulate fibrosis in fibroblast cells under conditions of critical size bone defects [81].

Evaluating the mechanical properties of newly formed bone tissue proved challenging due to the difficulty in removing the fixation plate from the bone in this critical size defect model. Consequently, we opted to assess pain and behavior [82,83] as indicators of mobility restoration in mice following treatment. As expected, mice subjected to angiogenic factor treatment exhibited significantly reduced stimulus-evoked nociception, as evidenced by von Frey and Small Animal Analgesiometer (SMALGO) assessments. Conversely, mice treated with the PCL scaffold alone demonstrated heightened sensitivity to mechanical allodynia, observed both at the plantar surface of the paw (von Frey) and at the site of the injured femur (SMALGO) (Fig. 7C and D). More importantly, when compared to treatment with the PCL scaffold alone, the administration of angiogenic factors significantly improved the mobility of mice with critical size bone defects, as reflected by reduced rest times and increased travel distances, as well as higher mean and maximum speeds observed in running wheels (Fig. 7E–H). Previous studies have

Table 1
Remaining growth factors in scaffolds after 3 and 14 days of implantation.

Day 3		Day 14	
Spp1 (%)	Cxcl12 (%)	Spp1 (%)	Cxcl12 (%)
78.4	53.0	69.4	30.3
68.9	53.1	57.7	62.7
64.6	55.9	57.6	37.2

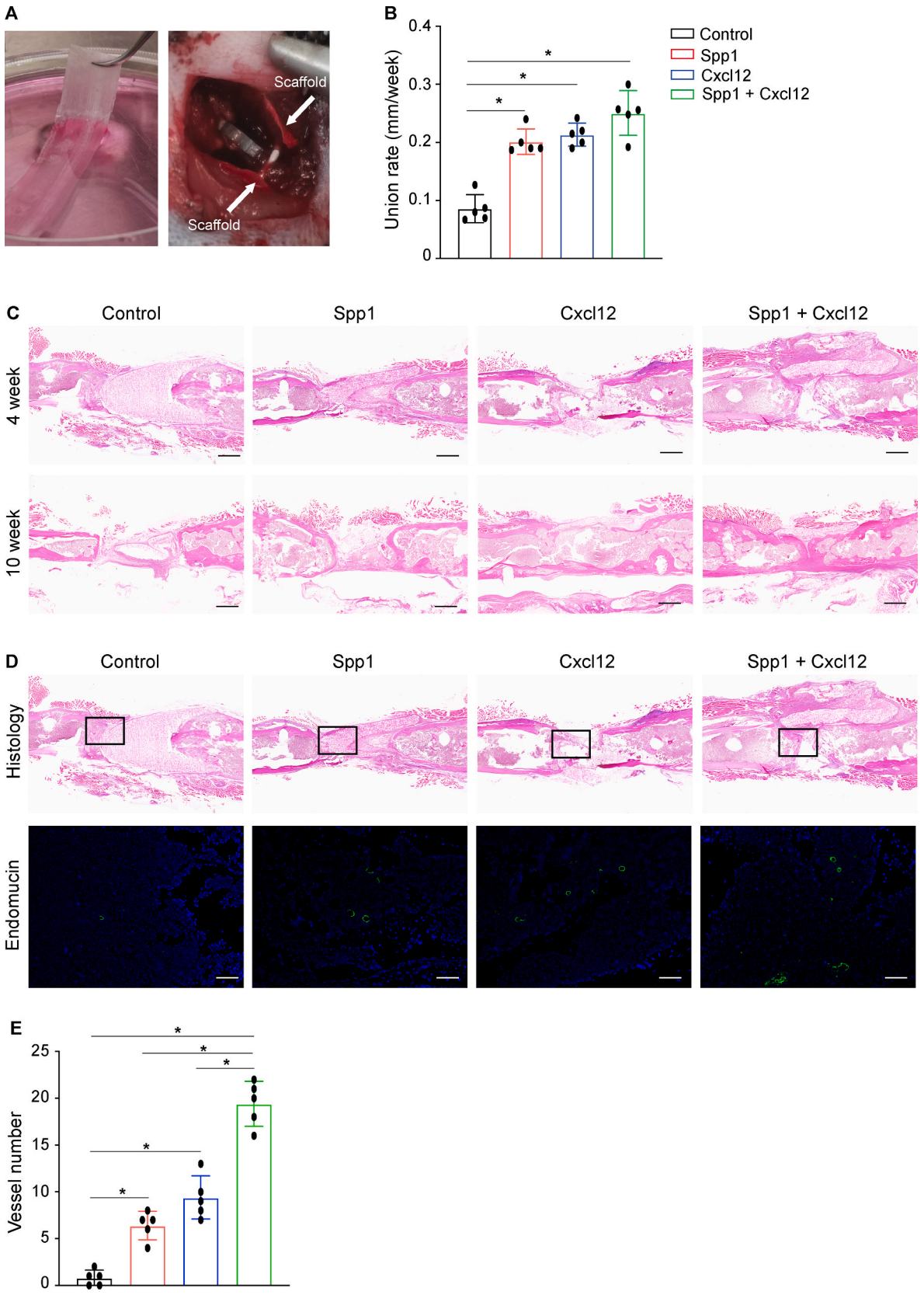

Fig. 6. Restored angiogenesis and bone regeneration in mice treated with Spp1 and Cxcl12. (**A**) PCL scaffolds with or without Spp1 and Cxcl12 was applied to the mice with critical size bone defects. (**B**) Quantification of bony tissue formation rate based on the in-vivo microCT scans over 10 weeks. (**C**) Representative ABH/OG staining of murine femurs with critical size bone defects treated with scaffold with or without Spp1 and Cxcl12 at 4 weeks and 10 weeks post-surgery. Scale bar, 500 μm. (**D**) Immunofluorescent staining for endomucin in regenerative tissues from critical size bone defects at 4 weeks post-surgery. Scale bar, 250 μm. (**E**) Quantifications of the vessels in regenerative tissues based on the immunohistochemical assessment (n = 5). Data presented as mean ± SD. *$p < 0.05$ by 2-way ANOVA followed by Tukey's test.

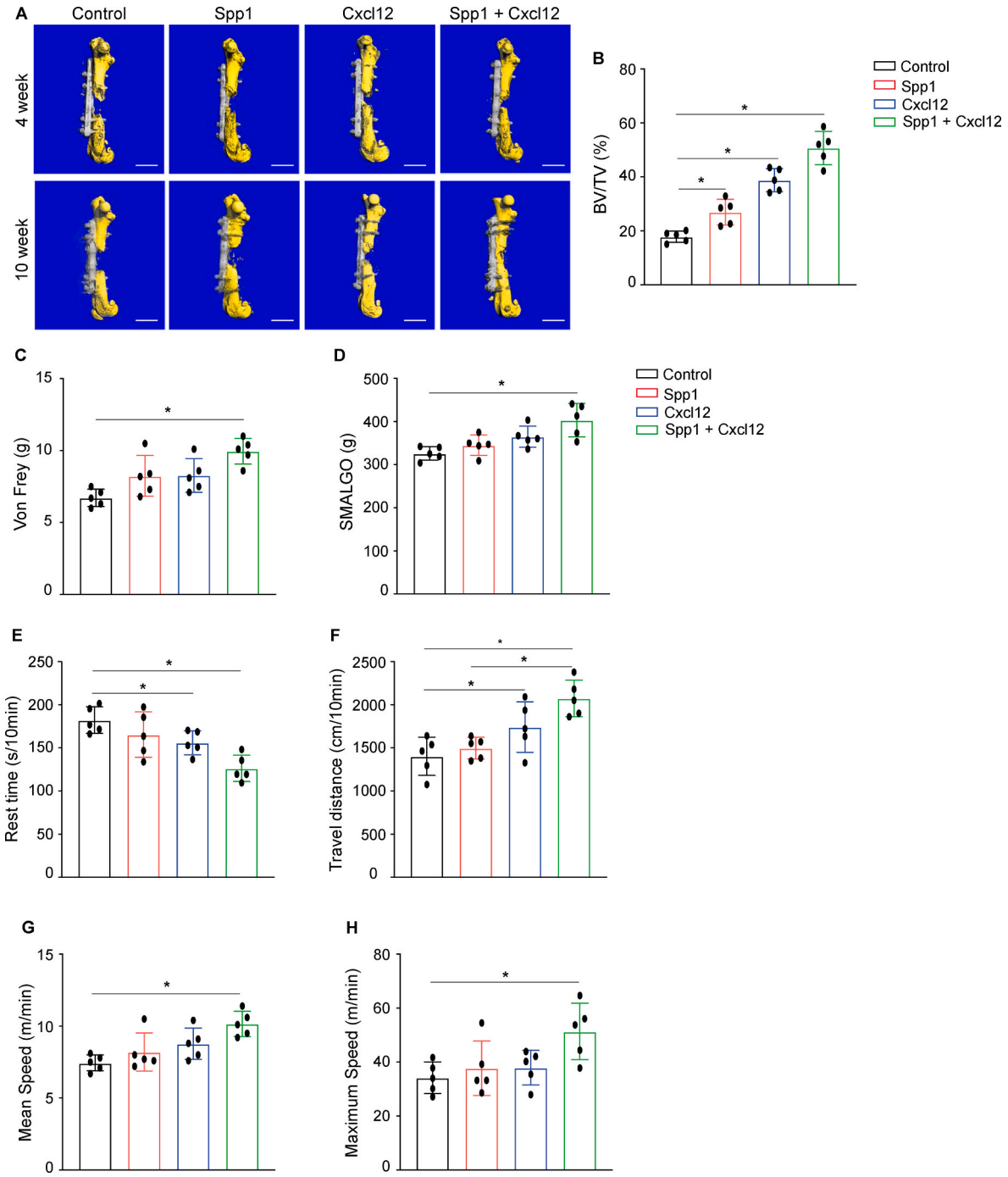

Fig. 7. Improved bone regeneration and alleviated pain responses in mice treated with Spp1 and Cxcl12. (**A**) microCT images of murine femurs with critical size bone defects at 4 weeks and 10 weeks post-surgery. Scale bar, 2 mm. (**B**) Quantification of BV/TV ratio based on the microCT scans at 10 weeks post-surgery (n = 5). The results were normalized to the scaffold only group. Pain responses were evaluated in mice with critical size bone defects treated with PCL scaffolds with or without Spp1 and Cxcl12 at 10 weeks post-surgery using (**C**) Von Frey and (**D**) SMALGO assays (n = 5). The mobility of mice with critical size bone defects treated with PCL scaffolds with or without Spp1 and Cxcl12 was recorded including (**E**) rest time, (**F**) travel distance, as well as (**G**) mean speed and (**H**) maximum speed in running wheels (n = 5). Data presented as mean ± SD. *$p < 0.05$ by 2-way ANOVA followed by Tukey's test.

highlighted the positive effects of exercise or mechanical stimulation on bone formation and regeneration in fracture scenarios. Therefore, we speculate that the alleviation of pain associated with critical size defects post-treatment enabled mice to improve their mobility, while appropriate mechanical cues further stimulated the osteogenic differentiation of progenitor cells and the bone regeneration process [84–86]. These findings strongly support the localized delivery of Spp1 and Cxcl12 via PCL scaffold as a potent therapeutic strategy for the clinical management of critical size bone defects.

4. Conclusion

Despite significant progress in therapeutics and surgical interventions, critical size bone defects remain as one of the most formidable challenges in orthopedic surgery. Current treatment modalities, such as bone graft implantation, the Masquelet technique, and distraction osteogenesis, are utilized; however, the limited availability of donor grafts necessitates exploration of alternative approaches. Tissue engineering holds promise in providing synthetic alternatives for treating

critical size bone defect. Nevertheless, a fundamental challenge in tissue engineering remains a barrier to successful translation and clinical outcomes: how to recreate microenvironments to control cell viability and cell fate effectively. To address this challenge, we employed single-cell RNA-seq to identify and profile individual cells, comprehensively delineating how critical size bone defects alter the cellular and molecular programs involved in bone regeneration. Our analysis revealed that diminished angiogenesis, mediated by Spp1 and Cxcl12, emerged as a converging pathway affected in several key cell lineages, including progenitor cells, endothelial cells and myeloid cells. Recognizing angiogenesis as a pivotal initial step to restore oxygen and nutrition in the bone defect microenvironment and to recruit various cells for bone regeneration, we developed a biomaterial capable of locally delivering Spp1 and Cxcl12 in a controllable manner. Our approach involved integrating electrospun PCL fibers with electrosprayed PLGA microspheres carrying Spp1 and Cxcl12, enabling gradual and sustained release of these factors in both in vitro and in vivo settings. Notably, local delivery of Spp1 and Cxcl12 via PCL scaffolds resulted in restored angiogenesis, accelerated bone regeneration, alleviated pain responses and improved mobility in mice with critical size bone defects. This comprehensive study offers promising insights into addressing the challenges associated with critical size bone defects and provides a novel therapeutic strategy for enhancing bone regeneration and improving patient outcomes.

Data availability

All relevant data associated with this work is available upon request. The scRNA-seq data generated in this study have been deposited in the Gene Expression Omnibus (GEO) database under accession GSE262544.

Ethics approval and consent to participate

All the animal experiments were performed in accordance with approval of the Committees on Animal Resources at Washington University in St. Louis.

CRediT authorship contribution statement

Liang Fang: Writing – original draft, Methodology, Investigation, Formal analysis, Data curation. **Zhongting Liu:** Writing – original draft, Methodology, Investigation, Formal analysis, Data curation. **Cuicui Wang:** Writing – review & editing, Investigation, Formal analysis, Data curation. **Meng Shi:** Investigation, Formal analysis. **Yonghua He:** Investigation, Formal analysis. **Aiwu Lu:** Investigation, Formal analysis. **Xiaofei Li:** Data curation. **Tiandao Li:** Data curation. **Donghui Zhu:** Data curation. **Bo Zhang:** Data curation. **Jianjun Guan:** Writing – review & editing, Writing – original draft, Validation, Supervision, Funding acquisition, Conceptualization. **Jie Shen:** Writing – review & editing, Writing – original draft, Validation, Supervision, Project administration, Funding acquisition, Conceptualization.

Declaration of competing interest

Donghui Zhu is an editorial board member for *Bioactive Materials* and was not involved in the editorial review or the decision to publish this article. All authors declare that there are no competing interests.

Acknowledgments

This work was supported by the following NIH grants: R01 grants (AR075860, AR077616, and AR083900 to JS; HL138175, HL164062, and DK133949 to JG) and a R21 grant (AR077226 to JS), and a P30 Core Center grant (AR074992 to the Musculoskeletal Research Center at Washington University in St. Louis).

Appendix A. Supplementary data

Supplementary data to this article can be found online at https://doi.org/10.1016/j.bioactmat.2024.07.003.

References

[1] A. Vajgel, N. Mardas, B.C. Farias, A. Petrie, R. Cimoes, N. Donos, A systematic review on the critical size defect model, Clin. Oral Implants Res. 25 (8) (2014) 879–893.
[2] E. Roddy, M.R. DeBaun, A. Daoud-Gray, Y.P. Yang, M.J. Gardner, Treatment of critical-sized bone defects: clinical and tissue engineering perspectives, Eur. J. Orthop. Surg. Traumatol. 28 (3) (2018) 351–362.
[3] A. Nauth, E. Schemitsch, B. Norris, Z. Nollin, J.T. Watson, Critical-size bone defects: is there a Consensus for Diagnosis and treatment? J. Orthop. Trauma 32 (Suppl 1) (2018) S7–S11.
[4] E.H. Schemitsch, Size Matters: Defining critical in bone defect size, J. Orthop. Trauma 31 (Suppl 5) (2017) S20–S22.
[5] A.H. Schmidt, Autologous bone graft: is it still the gold standard? Injury 52 (Suppl 2) (2021) S18–S22.
[6] M.P. Ferraz, Bone grafts in Dental medicine: an overview of Autografts, allografts and synthetic materials, Materials 16 (11) (2023).
[7] H.J. Haugen, S.P. Lyngstadaas, F. Rossi, G. Perale, Bone grafts: which is the ideal biomaterial? J. Clin. Periodontol. 46 (Suppl 21) (2019) 92–102.
[8] B.L. Norris, M. Vanderkarr, C. Sparks, A.S. Chitnis, B. Ray, C.E. Holy, Treatments, cost and healthcare utilization of patients with segmental bone defects, Injury 52 (10) (2021) 2935–2940.
[9] A.S. Brydone, D. Meek, S. Maclaine, Bone grafting, orthopaedic biomaterials, and the clinical need for bone engineering, Proc. Inst. Mech. Eng. H 224 (12) (2010) 1329–1343.
[10] H.S. Sohn, J.K. Oh, Review of bone graft and bone substitutes with an emphasis on fracture surgeries, Biomater. Res. 23 (2019) 9.
[11] N. Xue, X. Ding, R. Huang, R. Jiang, H. Huang, X. Pan, W. Min, J. Chen, J.A. Duan, P. Liu, Y. Wang, Bone tissue engineering in the treatment of bone defects, Pharmaceuticals 15 (7) (2022).
[12] A. Kengelbach-Weigand, C. Thielen, T. Bauerle, R. Gotzl, T. Gerber, C. Korner, J. P. Beier, R.E. Horch, A.M. Boos, Personalized medicine for reconstruction of critical-size bone defects - a translational approach with customizable vascularized bone tissue, NPJ Regen Med 6 (1) (2021) 49.
[13] B. Wildemann, A. Ignatius, F. Leung, L.A. Taitsman, R.M. Smith, R. Pesantez, M. J. Stoddart, R.G. Richards, J.B. Jupiter, Non-union bone fractures, Nat. Rev. Dis. Prim. 7 (1) (2021) 57.
[14] J. Ying, T. Xu, C. Wang, H. Jin, P. Tong, J. Guan, Y. Abu-Amer, R. O'Keefe, J. Shen, Dnmt3b ablation impairs fracture repair through upregulation of Notch pathway, JCI Insight 5 (3) (2020).
[15] C. Wang, J.A. Inzana, A.J. Mirando, Y. Ren, Z. Liu, J. Shen, R.J. O'Keefe, H. A. Awad, M.J. Hilton, NOTCH signaling in skeletal progenitors is critical for fracture repair, J. Clin. Invest. 126 (4) (2016) 1471–1481.
[16] M. Hadjiargyrou, R.J. O'Keefe, The convergence of fracture repair and stem cells: interplay of genes, aging, environmental factors and disease, J. Bone Miner. Res. 29 (11) (2014) 2307–2322.
[17] R.J. O'Keefe, Fibrinolysis as a target to enhance fracture healing, N. Engl. J. Med. 373 (18) (2015) 1776–1778.
[18] M. Jager, E.M. Jelinek, K.M. Wess, A. Scharfstadt, M. Jacobson, S.V. Kevy, R. Krauspe, Bone marrow concentrate: a novel strategy for bone defect treatment, Curr. Stem Cell Res. Ther. 4 (1) (2009) 34–43.
[19] A. Gianakos, A. Ni, L. Zambrana, J.G. Kennedy, J.M. Lane, Bone marrow Aspirate concentrate in animal long bone healing: an analysis of basic science evidence, J. Orthop. Trauma 30 (1) (2016) 1–9.
[20] M. Petri, A. Namazian, F. Wilke, M. Ettinger, T. Stubig, S. Brand, F. Bengel, C. Krettek, G. Berding, M. Jagodzinski, Repair of segmental long-bone defects by stem cell concentrate augmented scaffolds: a clinical and positron emission tomography–computed tomography analysis, Int. Orthop. 37 (11) (2013) 2231–2237.
[21] H. Hirata, N. Zhang, M. Ueno, D. Barati, J. Kushioka, H. Shen, M. Tsubosaka, M. Toya, T. Lin, E. Huang, Z. Yao, J.Y. Wu, S. Zwingenberger, F. Yang, S. B. Goodman, Ageing attenuates bone healing by mesenchymal stem cells in a microribbon hydrogel with a murine long bone critical-size defect model, Immun. Ageing 19 (1) (2022) 14.
[22] D. Medhat, C.I. Rodriguez, A. Infante, Immunomodulatory effects of MSCs in bone healing, Int. J. Mol. Sci. 20 (21) (2019).
[23] T. Zhao, Z.N. Zhang, Z. Rong, Y. Xu, Immunogenicity of induced pluripotent stem cells, Nature 474 (7350) (2011) 212–215.
[24] S. Schu, M. Nosov, L. O'Flynn, G. Shaw, O. Treacy, F. Barry, M. Murphy, T. O'Brien, T. Ritter, Immunogenicity of allogeneic mesenchymal stem cells, J. Cell Mol. Med. 16 (9) (2012) 2094–2103.
[25] H.G. Song, R.T. Rumma, C.K. Ozaki, E.R. Edelman, C.S. Chen, Vascular tissue engineering: progress, challenges, and clinical promise, Cell Stem Cell 22 (3) (2018) 340–354.
[26] S.K. Ramasamy, A.P. Kusumbe, M. Schiller, D. Zeuschner, M.G. Bixel, C. Milia, J. Gamrekelashvili, A. Limbourg, A. Medvinsky, M.M. Santoro, F.P. Limbourg, R. H. Adams, Blood flow controls bone vascular function and osteogenesis, Nat. Commun. 7 (2016) 13601.

[27] J. Zhang, J. Pan, W. Jing, Motivating role of type H vessels in bone regeneration, Cell Prolif. 53 (9) (2020) e12874.
[28] Y. Peng, S. Wu, Y. Li, J.L. Crane, Type H blood vessels in bone modeling and remodeling, Theranostics 10 (1) (2020) 426–436.
[29] J. Xu, S.J. He, T.T. Xia, Y. Shan, L. Wang, Targeting type H vessels in bone-related diseases, J. Cell Mol. Med. 28 (4) (2024) e18123.
[30] V. Mironov, R.P. Visconti, V. Kasyanov, G. Forgacs, C.J. Drake, R.R. Markwald, Organ printing: tissue spheroids as building blocks, Biomaterials 30 (12) (2009) 2164–2174.
[31] R.P. Visconti, V. Kasyanov, C. Gentile, J. Zhang, R.R. Markwald, V. Mironov, Towards organ printing: engineering an intra-organ branched vascular tree, Expet Opin. Biol. Ther. 10 (3) (2010) 409–420.
[32] J.S. Miller, K.R. Stevens, M.T. Yang, B.M. Baker, D.H. Nguyen, D.M. Cohen, E. Toro, A.A. Chen, P.A. Galie, X. Yu, R. Chaturvedi, S.N. Bhatia, C.S. Chen, Rapid casting of patterned vascular networks for perfusable engineered three-dimensional tissues, Nat. Mater. 11 (9) (2012) 768–774.
[33] D.B. Kolesky, R.L. Truby, A.S. Gladman, T.A. Busbee, K.A. Homan, J.A. Lewis, 3D bioprinting of vascularized, heterogeneous cell-laden tissue constructs, Adv. Mater. 26 (19) (2014) 3124–3130.
[34] D.B. Kolesky, K.A. Homan, M.A. Skylar-Scott, J.A. Lewis, Three-dimensional bioprinting of thick vascularized tissues, Proc. Natl. Acad. Sci. U.S.A. 113 (12) (2016) 3179–3184.
[35] C. Norotte, F.S. Marga, L.E. Niklason, G. Forgacs, Scaffold-free vascular tissue engineering using bioprinting, Biomaterials 30 (30) (2009) 5910–5917.
[36] A. Skardal, J. Zhang, G.D. Prestwich, Bioprinting vessel-like constructs using hyaluronan hydrogels crosslinked with tetrahedral polyethylene glycol tetracrylates, Biomaterials 31 (24) (2010) 6173–6181.
[37] J.M. Isner, T. Asahara, Angiogenesis and vasculogenesis as therapeutic strategies for postnatal neovascularization, J. Clin. Invest. 103 (9) (1999) 1231–1236.
[38] H.H. Song, K.M. Park, S. Gerecht, Hydrogels to model 3D in vitro microenvironment of tumor vascularization, Adv. Drug Deliv. Rev. 79–80 (2014) 19–29.
[39] S. Kim, H. Lee, M. Chung, N.L. Jeon, Engineering of functional, perfusable 3D microvascular networks on a chip, Lab Chip 13 (8) (2013) 1489–1500.
[40] D.H. Nguyen, S.C. Stapleton, M.T. Yang, S.S. Cha, C.K. Choi, P.A. Galie, C.S. Chen, Biomimetic model to reconstitute angiogenic sprouting morphogenesis in vitro, Proc. Natl. Acad. Sci. U.S.A. 110 (17) (2013) 6712–6717.
[41] P.A. Galie, D.H. Nguyen, C.K. Choi, D.M. Cohen, P.A. Janmey, C.S. Chen, Fluid shear stress threshold regulates angiogenic sprouting, Proc. Natl. Acad. Sci. U.S.A. 111 (22) (2014) 7968–7973.
[42] J.W. Song, L.L. Munn, Fluid forces control endothelial sprouting, Proc. Natl. Acad. Sci. U.S.A. 108 (37) (2011) 15342–15347.
[43] N. Zhang, C.W. Lo, T. Utsunomiya, M. Maruyama, E. Huang, C. Rhee, Q. Gao, Z. Yao, S.B. Goodman, PDGF-BB and IL-4 co-overexpression is a potential strategy to enhance mesenchymal stem cell-based bone regeneration, Stem Cell Res. Ther. 12 (1) (2021) 40.
[44] C.W. Pugh, P.J. Ratcliffe, Regulation of angiogenesis by hypoxia: role of the HIF system, Nat. Med. 9 (6) (2003) 677–684.
[45] G.L. Semenza, Hypoxia-inducible factors in physiology and medicine, Cell 148 (3) (2012) 399–408.
[46] S. Prado-Lopez, A. Conesa, A. Arminan, M. Martinez-Losa, C. Escobedo-Lucea, C. Gandia, S. Tarazona, D. Melguizo, D. Blesa, D. Montaner, S. Sanz-Gonzalez, P. Sepulveda, S. Gotz, J.E. O'Connor, R. Moreno, J. Dopazo, D.J. Burks, M. Stojkovic, Hypoxia promotes efficient differentiation of human embryonic stem cells to functional endothelium, Stem Cell. 28 (3) (2010) 407–418.
[47] Y. Han, Y. Wu, F. Wang, G. Li, J. Wang, X. Wu, A. Deng, X. Ren, X. Wang, J. Gao, Z. Shi, L. Bai, J. Su, Heterogeneous DNA hydrogel loaded with Apt02 modified tetrahedral framework nucleic acid accelerated critical-size bone defect repair, Bioact. Mater. 35 (2024) 1–16.
[48] K.A. Heintz, M.E. Bregenzer, J.L. Mantle, K.H. Lee, J.L. West, J.H. Slater, Fabrication of 3D Biomimetic Microfluidic networks in hydrogels, Adv. Healthcare Mater. 5 (17) (2016) 2153–2160.
[49] Z.S. Patel, S. Young, Y. Tabata, J.A. Jansen, M.E. Wong, A.G. Mikos, Dual delivery of an angiogenic and an osteogenic growth factor for bone regeneration in a critical size defect model, Bone 43 (5) (2008) 931–940.
[50] M. Wein, D. Huelter-Hassler, K. Nelson, T. Fretwurst, S. Nahles, G. Finkenzeller, B. Altmann, T. Steinberg, Differential osteopontin expression in human osteoblasts derived from iliac crest and alveolar bone and its role in early stages of angiogenesis, J. Bone Miner. Metabol. 37 (1) (2019) 105–117.
[51] G.C. Rowe, S. Raghuram, C. Jang, J.A. Nagy, I.S. Patten, A. Goyal, M.C. Chan, L. X. Liu, A. Jiang, K.C. Spokes, D. Beeler, H. Dvorak, W.C. Aird, Z. Arany, PGC-1alpha induces SPP1 to activate macrophages and orchestrate functional angiogenesis in skeletal muscle, Circ. Res. 115 (5) (2014) 504–517.
[52] S. Liekens, D. Schols, S. Hatse, CXCL12-CXCR4 axis in angiogenesis, metastasis and stem cell mobilization, Curr. Pharmaceut. Des. 16 (35) (2010) 3903–3920.
[53] C.L. Duvall, W.R. Taylor, D. Weiss, A.M. Wojtowicz, R.E. Guldberg, Impaired angiogenesis, early callus formation, and late stage remodeling in fracture healing of osteopontin-deficient mice, J. Bone Miner. Res. 22 (2) (2007) 286–297.
[54] M. Fujio, A. Yamamoto, Y. Ando, R. Shohara, K. Kinoshita, T. Kaneko, H. Hibi, M. Ueda, Stromal cell-derived factor-1 enhances distraction osteogenesis-mediated skeletal tissue regeneration through the recruitment of endothelial precursors, Bone 49 (4) (2011) 693–700.
[55] M. Manassero, A. Decambron, B.T. Huu Thong, V. Viateau, M. Bensidhoum, H. Petite, Establishment of a segmental femoral critical-size defect model in mice stabilized by plate Osteosynthesis, J. Vis. Exp. 116 (2016).
[56] D. Xiao, L. Fang, Z. Liu, Y. He, J. Ying, H. Qin, A. Lu, M. Shi, T. Li, B. Zhang, J. Guan, C. Wang, Y. Abu-Amer, J. Shen, DNA methylation-mediated Rbpjk suppression protects against fracture nonunion caused by systemic inflammation, J. Clin. Invest. 134 (3) (2023).
[57] Y. Hao, S. Hao, E. Andersen-Nissen, W.M. Mauck 3rd, S. Zheng, A. Butler, M.J. Lee, A.J. Wilk, C. Darby, M. Zager, P. Hoffman, M. Stoeckius, E. Papalexi, E.P. Mimitou, J. Jain, A. Srivastava, T. Stuart, L.M. Fleming, B. Yeung, A.J. Rogers, J. M. McElrath, C.A. Blish, R. Gottardo, P. Smibert, R. Satija, Integrated analysis of multimodal single-cell data, Cell 184 (13) (2021) 3573–3587 e29.
[58] J. Chen, B.J. Aronow, A.G. Jegga, Disease candidate gene identification and prioritization using protein interaction networks, BMC Bioinf. 10 (2009) 73.
[59] A. Subramanian, P. Tamayo, V.K. Mootha, S. Mukherjee, B.L. Ebert, M.A. Gillette, A. Paulovich, S.L. Pomeroy, T.R. Golub, E.S. Lander, J.P. Mesirov, Gene set enrichment analysis: a knowledge-based approach for interpreting genome-wide expression profiles, Proc. Natl. Acad. Sci. U.S.A. 102 (43) (2005) 15545–15550.
[60] T. Xu, C. Wang, J. Shen, P. Tong, R. O'Keefe, Ablation of Dnmt3b in chondrocytes suppresses cell maturation during embryonic development, J. Cell. Biochem. 119 (7) (2018) 5852–5863.
[61] C. Wang, J. Shen, K. Yukata, J.A. Inzana, R.J. O'Keefe, H.A. Awad, M.J. Hilton, Transient gamma-secretase inhibition accelerates and enhances fracture repair likely via Notch signaling modulation, Bone 73 (2015) 77–89.
[62] C. Wang, Y. Abu-Amer, R.J. O'Keefe, J. Shen, Loss of Dnmt3b in chondrocytes leads to Delayed endochondral ossification and fracture repair, J. Bone Miner. Res. 33 (2) (2018) 283–297.
[63] X. Guo, C.G. Elliott, Z. Li, Y. Xu, D.W. Hamilton, J. Guan, Creating 3D angiogenic growth factor gradients in fibrous constructs to guide fast angiogenesis, Biomacromolecules 13 (10) (2012) 3262–3271.
[64] Y. Xu, S. Patnaik, X. Guo, Z. Li, W. Lo, R. Butler, A. Claude, Z. Liu, G. Zhang, J. Liao, P.M. Anderson, J. Guan, Cardiac differentiation of cardiosphere-derived cells in scaffolds mimicking morphology of the cardiac extracellular matrix, Acta Biomater. 10 (8) (2014) 3449–3462.
[65] C. Wang, J. Ying, X. Nie, T. Zhou, D. Xiao, G. Swarnkar, Y. Abu-Amer, J. Guan, J. Shen, Targeting angiogenesis for fracture nonunion treatment in inflammatory disease, Bone Res 9 (1) (2021) 29.
[66] L. Zhong, L. Yao, R.J. Tower, Y. Wei, Z. Miao, J. Park, R. Shrestha, L. Wang, W. Yu, N. Holdreith, X. Huang, Y. Zhang, W. Tong, Y. Gong, J. Ahn, K. Susztak, N. Dyment, M. Li, F. Long, C. Chen, P. Seale, L. Qin, Single cell transcriptomics identifies a unique adipose lineage cell population that regulates bone marrow environment, Elife 9 (2020).
[67] K.A. Pulford, A. Sipos, J.L. Cordell, W.P. Stross, D.Y. Mason, Distribution of the CD68 macrophage/myeloid associated antigen, Int. Immunol. 2 (10) (1990) 973–980.
[68] M. Corada, F. Liao, M. Lindgren, M.G. Lampugnani, F. Breviario, R. Frank, W. A. Muller, D.J. Hicklin, P. Bohlen, E. Dejana, Monoclonal antibodies directed to different regions of vascular endothelial cadherin extracellular domain affect adhesion and clustering of the protein and modulate endothelial permeability, Blood 97 (6) (2001) 1679–1684.
[69] C. Schlundt, T. El Khassawna, A. Serra, A. Dienelt, S. Wendler, H. Schell, N. van Rooijen, A. Radbruch, R. Lucius, S. Hartmann, G.N. Duda, K. Schmidt-Bleek, Macrophages in bone fracture healing: their essential role in endochondral ossification, Bone 106 (2018) 78–89.
[70] R. Pawar, A. Pathan, S. Nagaraj, H. Kapare, P. Giram, R. Wavhale, Polycaprolactone and its derivatives for drug delivery, Polym. Adv. Technol. 34 (10) (2023) 3296–3316.
[71] P.K. Petrow, K.M. Hummel, J. Schedel, J.K. Franz, C.L. Klein, U. Muller-Ladner, J. Kriegsmann, P.L. Chang, C.W. Prince, R.E. Gay, S. Gay, Expression of osteopontin messenger RNA and protein in rheumatoid arthritis: effects of osteopontin on the release of collagenase 1 from articular chondrocytes and synovial fibroblasts, Arthritis Rheum. 43 (7) (2000) 1597–1605.
[72] K.W. Kim, M.L. Cho, H.R. Kim, J.H. Ju, M.K. Park, H.J. Oh, J.S. Kim, S.H. Park, S. H. Lee, H.Y. Kim, Up-regulation of stromal cell-derived factor 1 (CXCL12) production in rheumatoid synovial fibroblasts through interactions with T lymphocytes: role of interleukin-17 and CD40L-CD40 interaction, Arthritis Rheum. 56 (4) (2007) 1076–1086.
[73] P.H. Anborgh, J.C. Mutrie, A.B. Tuck, A.F. Chambers, Role of the metastasis-promoting protein osteopontin in the tumour microenvironment, J. Cell Mol. Med. 14 (8) (2010) 2037–2044.
[74] X. Sun, G. Cheng, M. Hao, J. Zheng, X. Zhou, J. Zhang, R.S. Taichman, K.J. Pienta, J. Wang, CXCL12/CXCR4/CXCR7 chemokine axis and cancer progression, Cancer Metastasis Rev. 29 (4) (2010) 709–722.
[75] L.A. Shevde, R.S. Samant, Role of osteopontin in the pathophysiology of cancer, Matrix Biol. 37 (2014) 131–141.
[76] A. Guyon, CXCL12 chemokine and its receptors as major players in the interactions between immune and nervous systems, Front. Cell. Neurosci. 8 (2014) 65.
[77] J. Sodek, J. Chen, T. Nagata, S. Kasugai, R. Todescan Jr., I.W. Li, R.H. Kim, Regulation of osteopontin expression in osteoblasts, Ann. N. Y. Acad. Sci. 760 (1995) 223–241.
[78] Y.S. Tzeng, N.C. Chung, Y.R. Chen, H.Y. Huang, W.P. Chuang, D.M. Lai, Imbalanced osteogenesis and Adipogenesis in mice deficient in the chemokine Cxcl12/Sdf1 in the bone mesenchymal stem/progenitor cells, J. Bone Miner. Res. 33 (4) (2018) 679–690.
[79] W. Zhu, G. Liang, Z. Huang, S.B. Doty, A.L. Boskey, Conditional inactivation of the CXCR4 receptor in osteoprecursors reduces postnatal bone formation due to impaired osteoblast development, J. Biol. Chem. 286 (30) (2011) 26794–26805.
[80] A. Faqeer, M. Wang, G. Alam, A.A. Padhiar, D. Zheng, Z. Luo, I.S. Zhao, G. Zhou, J. van den Beucken, H. Wang, Y. Zhang, Cleaved SPP1-rich extracellular vesicles

from osteoclasts promote bone regeneration via TGFbeta1/SMAD3 signaling, Biomaterials 303 (2023) 122367.
[81] K. Hoeft, G.J.L. Schaefer, H. Kim, D. Schumacher, T. Bleckwehl, Q. Long, B. M. Klinkhammer, F. Peisker, L. Koch, J. Nagai, M. Halder, S. Ziegler, E. Liehn, C. Kuppe, J. Kranz, S. Menzel, I. Costa, A. Wahida, P. Boor, R.K. Schneider, S. Hayat, R. Kramann, Platelet-instructed SPP1(+) macrophages drive myofibroblast activation in fibrosis in a CXCL4-dependent manner, Cell Rep. 42 (2) (2023) 112131.
[82] V. Minville, J.M. Laffosse, O. Fourcade, J.P. Girolami, I. Tack, Mouse model of fracture pain, Anesthesiology 108 (3) (2008) 467–472.
[83] R. Magnusdottir, S. Gohin, F. Ter Heegde, M. Hopkinson, I.F. McNally, A. Fisher, N. Upton, A. Billinton, C. Chenu, Fracture-induced pain-like behaviours in a femoral fracture mouse model, Osteoporos. Int. 32 (11) (2021) 2347–2359.
[84] A.G. Robling, C.H. Turner, Mechanical signaling for bone modeling and remodeling, Crit. Rev. Eukaryot. Gene Expr. 19 (4) (2009) 319–338.
[85] L. Wang, X. You, L. Zhang, C. Zhang, W. Zou, Mechanical regulation of bone remodeling, Bone Res 10 (1) (2022) 16.
[86] L. Song, Effects of exercise or mechanical stimulation on bone development and bone repair, Stem Cell. Int. (2022) 5372229, 2022.